

The following publication Zhang, H., Wang, H., Qian, P. C., & Wong, W. Y. (2020). A combination of an organic alloy and a heterojunction towards a rod-tail helix architecture with dual-color-emitting properties. *Nanoscale*, 12(31), 16414-16419 is available at <https://doi.org/10.1039/d0nr03948a>.

# Combination of organic alloy and heterojunction towards rod-tail helix architecture with dual-color-emitting property

Hongyang Zhang,<sup>a,b</sup> Haitao Wang,<sup>b</sup> Peng-Cheng Qian,<sup>\*c</sup> and Wai-Yeung Wong<sup>\*a,b</sup>

**Organic alloy can be regarded as the homogeneous solid solution where the isostructural molecule is randomly distributed in the host molecule, compared to the organic heterojunction where the dissimilar materials generate the interface between two layers or regions. Herein, we fabricate an unprecedented novel BA@BA<sub>0.72</sub>BN<sub>0.28</sub> heterostructure with rod-tail helix configuration, in which the helical dual-component BA<sub>0.72</sub>BN<sub>0.28</sub> alloy can be grown in a controllable manner onto the mono-component BA microrod, forming the organic core-shell micro-structure. Especially, the process of the co-assembly formed could be described as the combined construction of organic alloy and heterojunction, and the co-assembly possesses the distinctive property of dual-color luminescence. This complex heterostructured architecture is achieved through a stepwise seed-induced growth method and the present solution-phase route allows us to construct more sophisticated organic luminescent heterostructured materials.**

## 1. Introduction

Organic heterojunction has always been an attractive research topic on account of its unique property and superior performance in the applications of lasers,<sup>1</sup> bipolar transistors,<sup>2</sup> field effect transistors,<sup>3</sup> solar cells<sup>4</sup> and organic light-emitting devices.<sup>5</sup> Notably, the construction of heterojunction at the nano- or micro-scale is an emerging field and remains a great challenge owing to the complicated dynamic assembly feature of each of the organic components. The process of fabrication is associated with the precise spatial manipulation of different constituent materials. The resultant heterojunction possesses nano- or micro-scaled structural

feature with the realization of increasingly elaborate performance, due to the synergistic effects with predefined constituent distribution.<sup>6</sup> On the other hand, organic alloy could be regarded as homogeneous solid mixtures, and specifically, the isostructural organic guest molecules are randomly dispersed into the crystal lattice of organic host molecules over a wide range of proportions.<sup>7</sup> This not only can unite the advantages of each organic component, but also bring improved and/or unexpected properties via a broad and continuous variation in chemical composition. For example, organic alloys of TSeF<sub>x</sub>TTF<sub>1-x</sub>TCNQ were synthesized by substitution of a TTF donor with another isostructural TSeF donor, and the value of *x* is permitted to vary from 0 to 1 to achieve variable electrical properties.<sup>8</sup> Applying a supramolecular approach to prepare three- or four-component organic alloys and further investigation on the modulation of their physical properties by gradual alteration of the constituent ratio was also reported.<sup>9</sup> Moreover, the organic alloy are also utilized for the applications of ambipolar organic thin film transistors as well as organic solar cells.<sup>10</sup>

Controlled synthesis of sophisticated heterogeneous architecture remains to be a large difficulty, especially for organic constituent materials. Actually, great efforts have been made, for instance, linear heterostructured nanotubes with dissimilar semiconducting properties were achieved by stepwise assembly of two graphene derivatives.<sup>11</sup> Moreover, crystalline heterojunction nanorods composed of Ir(III) and Ru(III) metallophosphors were developed via a similar stepwise growth approach.<sup>12</sup> Recently, our group has achieved the controlled formation of supramolecular core-shell heterostructures with multicolor optical performance<sup>13</sup> as well as facet-selective growth of organic heterostructured architectures by sequential crystallization.<sup>14</sup> In the previous works, it has been revealed that choosing the structural compatible materials and appropriately tuning their growth kinetics is the key to construct the complex organic heterostructures.

The integration of organic alloy into organic heterojunction has been rarely reported due to the difficulty in simultaneously producing the alloy and controlling the growth kinetics of the alloy on the seeded material. Herein, based on the complex assembly of planar and twisted  $\pi$ -conjugated molecules towards organic alloy,<sup>15</sup> we further develop an unprecedented heterogeneous rod-tail helix

<sup>a</sup> Department of Applied Biology and Chemical Technology, The Hong Kong Polytechnic University, Hung Hom, Hong Kong, China.

E-mail: wai-yeung.wong@polyu.edu.hk

<sup>b</sup> Department of Chemistry, Hong Kong Baptist University, Waterloo Road, Hong Kong, China.

<sup>c</sup> Key Laboratory of Environmental Functional Materials Technology and Application of Wenzhou City, Institute of New Materials & Industry, College of Chemistry & Materials Engineering, Wenzhou University, Wenzhou 325035, China. E-mail: qpc@wzu.edu.cn

configuration, i.e.  $BA@BA_{0.72}BN_{0.28}$ , with a core-shell organic structure constructed by a two-step seeded-induced growth approach, and the organic alloy shell is composed of two isostructural semiconductor molecules, BA and BN, through  $\pi$ - $\pi$  interaction. In contrast to the dual-component shell, the core rod comprises single BA molecule. During the formation process, the alloy shell  $BA_{0.72}BN_{0.28}$  first deposits on the side face of BA core via a solution epitaxial growth,<sup>17</sup> then the ribbon-shaped shell extends out with screwing into bundles of helices, finally forming the structure with the rod-tail helical shape.

## 2. Results and discussion

Two structural similar  $\pi$ -conjugated molecules, 9,10-bis(phenylethynyl)anthracene (BA) and 5,12-bis(phenylethynyl)naphthacene (BN) (Fig. 1a) are chosen to explore the fabrication of organic alloy as well as its novel heterostructure. Under the specific preparation condition ( $v/v = 4:1$ , ethanol/ $H_2O$  solvent mixture), the individual assemblies of these two isostructural molecules possess two slightly different morphologies. Specifically, BA can assemble into partial hollow microrods (Fig. 1b, e and Fig S1, ESI<sup>†</sup>), while BN can assemble into hollow microtubes (Fig. 1c, f). By contrast, BA and BN can co-assemble into organic alloy helices (Fig. 1d, g & Fig S2, ESI<sup>†</sup>) under the same synthetic conditions because the BA-BN dimeric units can be consistently twisted towards one joint direction which would be a preferable strategy of decreasing the total free energy in the co-assembly system. The BN guest can occupy the sites in which the BA host provides, and form the specific composition  $BA_{0.72}BN_{0.28}$ , which has been confirmed in our previous work.<sup>15</sup>

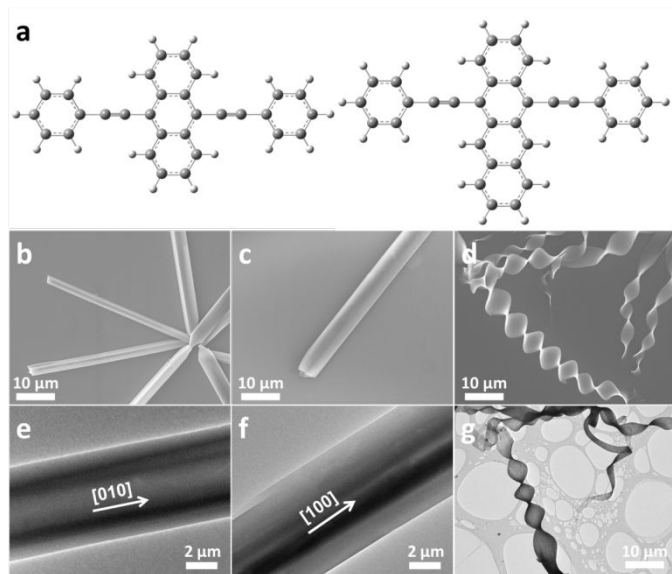


**Figure 1.** (a) Schematic showing the BA and BN molecular structures. (b,e) SEM and TEM images of microrods composed of single component: BA. (c,f) SEM and TEM images of microtubes composed of single component: BN. (d,g) SEM and TEM images of organic alloy helices composed of BA and BN components:  $BA_{0.72}BN_{0.28}$ .

Instead of applying the simple solute exchange method for the fabrication of simple core-shell structure, a complex core-shell structure,  $BA@BA_{0.72}BN_{0.28}$ , was designed and developed here via a stepwise seed-induced growth method. The growth mechanism can be explicated by the epitaxy process besides the structural analyses of BA crystal and BA/BN alloy crystal (Fig. S4a, b, ESI<sup>†</sup>). As we have investigated previously, it is hard to recognize BN molecules from the crystal lattice of BA in alloys because BN molecules would be randomly located at the sites provided by BA host, and thus the two-component organic alloy crystal exhibits similar molecular configuration relative to the pure BA crystal, in which the planar BA and twisted BN molecules are stacked together by strong  $\pi$ - $\pi$  interaction (Fig. S4c, d, ESI<sup>†</sup>).<sup>16</sup> Reasonably, the mono-component molecular stacking mode favors the formation of 1D morphology, therefore with the existence of BA rod-like seed and the well match between the lattices of seed and second growing alloy constituent, the first step, epitaxial growth occurs,<sup>17</sup> with the ribbon-shaped alloy shell  $BA_{0.72}BN_{0.28}$  growing on the BA seed entirely with the remaining shown as the rod figure. Next, the second step occurs, the surplus shell would extend out and it would be influenced by its own intermolecular force for recurring into a helical shape, finally leading to the core-shell construction of the rod-tail helix architecture (Fig. 2). Here, the intermolecular force refers to the BA-BN dimeric units consistently twisting towards the same direction, thereby resulting in a helical superstructure for the sake of reducing the total free energy in the alloy system.<sup>18</sup>

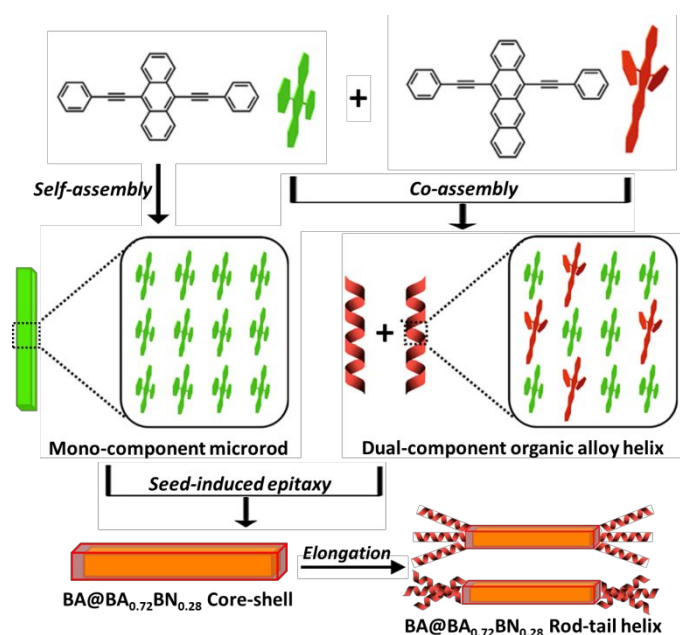


**Figure 2.** Schematic illustration of the growth mechanism of  $BA@BA_{0.72}BN_{0.28}$  rod-tail helix and the molecular packing of  $BA_{0.72}BN_{0.28}$  alloy helix, in which the BA host molecules are randomly replaced by the BN molecules and a BA-BN dimeric structure with a slight twist is formed.

During the detailed preparation process, the pre-synthetic BA microrods acted as the seed and dispersed under the same

synthetic condition for all of these self- and co-assemblies ( $v/v = 4:1$ , ethanol/ $H_2O$  solvent mixture, 5 mL), by means of fast injection of 1 mL stock solution of BA/BN in THF with a 2:1 molar ratio ( $C_{BA} = 5$  mM,  $C_{BN} = 2.5$  mM) and then gentle shaking of the mixed solution, a large number of heterogeneous core-shell microstructure,  $BA@BA_{0.72}BN_{0.28}$ , would be synthesized in the solution system (Fig. 3a). SEM characterization shows the specific topological configuration (Fig. 3b, c). From the TEM images (Fig. 3d, e), we could compare the thickness of the outside shell with the diameter of the inside core, which is about 1:1 in the length ratio (More SEM and TEM images of  $BA@BA_{0.72}BN_{0.28}$  are shown in Fig. S5, ESI<sup>†</sup>). Besides, in order to get more direct evidence to identify the core-shell fabrication, fluorescence microscopy tests were performed to examine the configuration because the core and shell can be distinguished by their different emission colors. Figure 3f, g exhibit the corresponding FM images excited by a blue laser, and as expected, the red-emitting layer is deposited onto the surface of a green-emitting core. The elongated helical ribbon emits the same color of light as the shell layer covered on the core rod. From a large view scale we can see this is not a specially observed sample on a partial position, but a universal synthetic success on the whole domain (Fig. 3h, i).

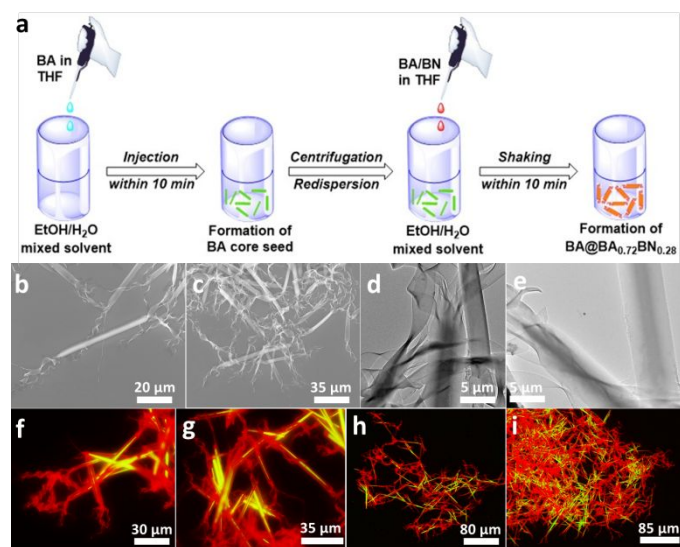


**Figure 3.** (a) Schematic illustration of the synthetic procedure of  $BA@BA_{0.72}BN_{0.28}$  rod-tail helix, (b-c) SEM images of  $BA@BA_{0.72}BN_{0.28}$  rod-tail helix (viewed from single to multiple). (d-e) TEM images of  $BA@BA_{0.72}BN_{0.28}$  rod-tail helix (viewed from tail to rod). (f-i) Fluorescence microscopy images of  $BA@BA_{0.72}BN_{0.28}$  rod-tail helix upon excitation with the blue laser (viewed from small to large).

In order to fully identify the distinctions of these assemblies and co-assemblies, their photophysical properties were first measured. With the aid of solid photoluminescent spectra, we can see that the emission band of  $BA_{0.72}BN_{0.28}$  alloy (665 nm) is located between the emission bands of BA microrods (550 nm) and BN microtubes (710 nm). Notably, the PL spectrum of  $BA@BA_{0.72}BN_{0.28}$  core-shell structure can be regarded as the spectral superposition of

separated BA assembly and  $BA_{0.72}BN_{0.28}$  alloy (Fig. 4a). This result not only confirms the core-shell fabrication but also implies the content of BA and  $BA_{0.72}BN_{0.28}$  depending on their luminescent intensities. The emission and excitation spectra of BA monomer solution, BN monomer solution and BA/BN precursor solutions in different concentrations (Fig. S6 & S7, ESI<sup>†</sup>) were also measured to demonstrate the strong  $\pi$ - $\pi$  interaction among these  $\pi$ -conjugated molecules, and the details are discussed in the ESI. Then, the powder X-ray diffraction (XRD) tests of these four assemblies were performed to reveal the internal structural information. Obviously, the XRD pattern of  $BA_{0.72}BN_{0.28}$  helix (Fig. 4b, blue curve) exhibits a pattern of the newly formed crystal phase, which is different from pure BA (Fig. 4b, red curve) and BN (Fig. 4b, black curve). New generated peaks at  $7.6^\circ$  and  $10.4^\circ$  not only indicate high-quality crystallinity but also reveal the alloy nature of the crystal phase. Then for the pattern of rod-tail helix heterostructure,  $BA@BA_{0.72}BN_{0.28}$ , it is completely the overlapping of peaks that are attributed to BA and  $BA_{0.72}BN_{0.28}$ , therefore this also can be looked upon as the direct evidence of the formation of heterostructured architecture. Furthermore, we explored their thermal stabilities and found that the decomposition temperature of pure BA is higher than that of organic alloy  $BA_{0.72}BN_{0.28}$ , probably due to a small amount of BN molecule incorporated into the alloy system whose thermal stability is slightly inferior to the BA molecule. The TGA plot of  $BA@BA_{0.72}BN_{0.28}$  is exactly situated between the curves of separate BA and  $BA_{0.72}BN_{0.28}$ , suggesting the composition of rod-tail helix heterojunction is just the combination of two materials, which is the indirect evidence of the formation of heterostructured architecture (Fig. 4c). Then laser confocal fluorescence microscopy (LCFM) is employed to record the shape, emission and morphology of BA microrod (Fig. 4d), BN microtube (Fig. 4e),  $BA_{0.72}BN_{0.28}$  helix (Fig. 4f) and  $BA@BA_{0.72}BN_{0.28}$  rod-tail helix (Fig. 4g), respectively. By sight, the construction of heterostructured architecture can be directly perceived.

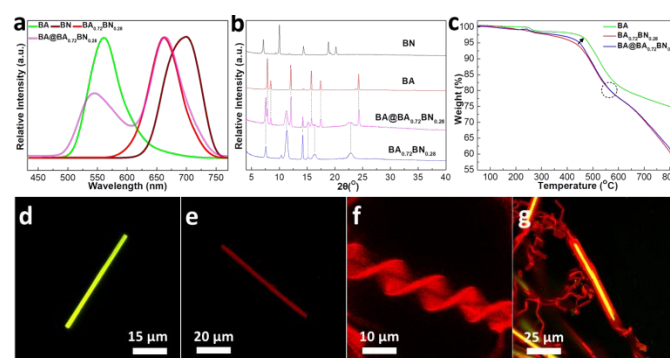


**Figure 4.** (a) Solid-state emission spectra of BA, BN,  $BA_{0.72}BN_{0.28}$  and  $BA@BA_{0.72}BN_{0.28}$  assemblies upon excitation with the blue laser ( $\lambda_{ex} = 405$  nm), (b) Powder XRD patterns of BA, BN,  $BA_{0.72}BN_{0.28}$  and  $BA@BA_{0.72}BN_{0.28}$  assemblies, (c). Thermogravimetric analysis (TGA) plots of BA,  $BA_{0.72}BN_{0.28}$ ,  $BA@BA_{0.72}BN_{0.28}$  assemblies, (d-g). Laser confocal fluorescence microscopic (LCFM) images of BA rod, BN tube,  $BA_{0.72}BN_{0.28}$  helix and  $BA@BA_{0.72}BN_{0.28}$  rod-tail helix.

Laser confocal fluorescence microscopy (LCFM) was further applied to evaluate the formed core-shell heterojunction from both qualitative and quantitative perspectives. The individual records of emission on the core (Fig. 5b, e) and shell (Fig. 5c, f) were conducted, respectively, and their merged emitting images were also provided (Fig. 5a, d). As we recorded the green light emitted from the core rod, the luminescence signal from the outside shell could not be detected, while as we collected the red emission of the shell layer, the emission of the inside core would turn off. The corresponding micro-area PL spectrum of BA@BA<sub>0.72</sub>BN<sub>0.28</sub> at the core-shell junction (marked in the white rectangle, Fig. 5d) shows a PL peak at 546 nm in the short-wavelength range and a PL peak at 665 nm in the long-wavelength range, which is exactly the superposition of the peaks of separate BA rod and BA/BN alloy. The intensities of the emission peaks also imply the content of two components on the whole heterostructure (Fig. 5g). By focusing on the PL peak on the middle section of the core-shell structure (marked in the white rectangle, Fig. 5e), we found that it shares the analogous spectral profile of two peaks but with different peak intensity. The PL peak at 546 nm caused by the inner BA core is higher than the peak at 661 nm derived from outer shell. This not only indicates that the middle section is composed of two constituent materials, but also gives the information of composition variation, in which the BA content rises at the middle section (Fig. 5h). Regarding the micro-area PL spectrum at the tip tail (marked in the white rectangle, Fig. 5f), it is the typical profile of BA/BN alloy helix with a single peak at 663 nm (Fig. 5i). Therefore, the above results adequately testify the formation of BA@BA<sub>0.72</sub>BN<sub>0.28</sub> core-shell heterostructure.

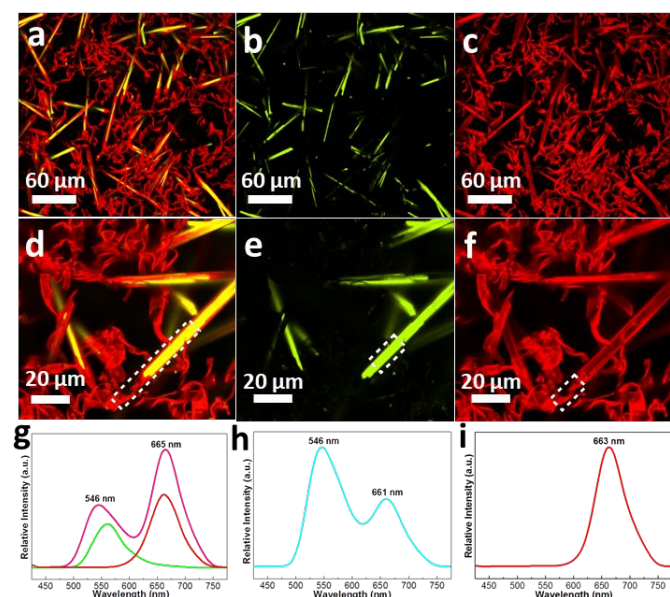


**Figure 5.** (a-c) LCFM images of core-shell rod-tail helix heterojunction BA@BA<sub>0.72</sub>BN<sub>0.28</sub> at a low magnification when collecting the green-light, red-light, and the merged emitting image, respectively; (d-f) LCFM images of core-shell rod-tail helix heterojunction BA@BA<sub>0.72</sub>BN<sub>0.28</sub> at a high magnification when collecting the green-light, red-light, and the merged emitting image,

respectively; (h-i) Micro-area PL spectra recorded from the selected areas on the rod-tail helix heterojunction BA@BA<sub>0.72</sub>BN<sub>0.28</sub> marked in the white rectangle in (d-f).

Additionally we selected a locally enlarged position under laser confocal fluorescence microscopy (LCFM, Fig. 6a-c) and took the emission images to record the continuously varying process of increasing the emission wavelength at 500, 550, 600, 650 and 700 nm respectively, in which the output signal was modified to the corresponding emitting color (Fig. 6d). Obviously, the emission range of the inner core is concentrated at 550 nm, by comparison, the emission range of the outer shell and tail helix are focused at around 650 nm. During the transitional region at 600 nm, basically no emitting materials are shown under our vision, while the emissions are relatively weak at 500 and 700 nm as well. The emitting properties on the specific wavelengths are in accordance with the feature of heterostructure. Thus far, the current characterizations have comprehensively supported the successful growth of dual-component organic alloy helix onto mono-component microrod towards rod-tail helix heterostructure from qualitative, quantitative, static and dynamic perspectives. Moreover, the organic helical organization is expected to exhibit superior optoelectronic performance,<sup>19</sup> such as for circularly polarized luminescence (CPL).<sup>20</sup> Although both left- and right-handed helices are found in our prepared system (Fig. S2b, ES1<sup>+</sup>), the final product should be a racemic mixture because achiral BA and BN were used as the building blocks. The circular dichroism (CD) spectrum also reveals the presence of a racemic mixture (Fig. S3, ES1<sup>+</sup>). It will be of great interest to explore the CPL based on the separation of chiral helices, and further work will be focused on this potential application in the optoelectronic field.

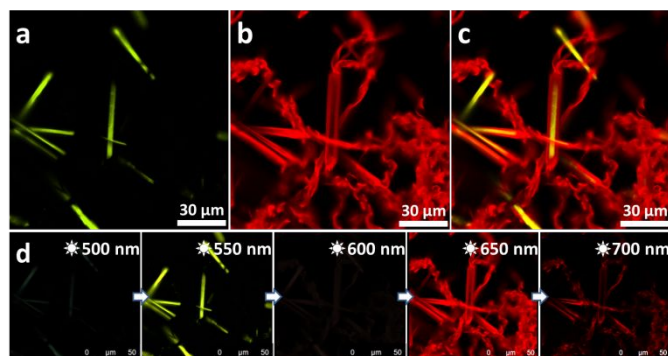


**Figure 6.** (a-c) Locally enlarged LCFM images of core-shell rod-tail helix: BA@BA<sub>0.72</sub>BN<sub>0.28</sub> when collecting green-light, red-light and the merged image of emission, respectively. (d) Emission images as a function of increasing wavelength.

### 3. Conclusions

A complex organic heterostructure with novel topological configuration was designed and fabricated through a stepwise seed-induced assembly process, wherein the organic alloy BA<sub>0.72</sub>BN<sub>0.28</sub> would wrap up the BA seed and spread out at the

tip to turn into its original helical morphology, which finally forms rod-tail helix architecture. The random occupancy of twisted BN guest at the sites of BA host makes little effect on the configuration of intermolecular stacking. This enables the perfect lattice matching between BA and BA<sub>0.72</sub>BN<sub>0.28</sub>, and provides the possibility for desired growth of organic alloy on the performed mono-component seed. The present successful case for constructing elaborated heterostructure sets up a bridge between organic alloy and organic heterojunction, and it could let us harness both the advantages of these two materials. As an inspiration, this synthetic approach also provides a promising platform to understand the structural relationship among varied but congenetic organic materials, and can be considered as a general pathway for realizing more sophisticated heterostructured architectures.

## Conflicts of interest

The authors declare no competing financial interest.

## Acknowledgements

W.-Y.W. acknowledges the financial support from the Hong Kong Research Grants Council (PolyU153062/18P), The Hong Kong Polytechnic University (1-ZE1C) and Ms Clarea Au for the Endowed Professorship in Energy (847S). PCQ thanks the Foundation of Wenzhou Science & Technology Bureau (No. W20170003) and the National Natural Science Foundation of China (No. 21828102).

## Notes and references

- H. Kroemer, *Proc. IEE.* 1963, **51**, 1782–1783.
- (a) G. L. Patton, S. S. Iyer, S. L. Delage, S. Tiwari, J. M. C. Stork, *Proc. IEE.* 1988, **9**, 165–167. (b) S. S. Iyer, G. L. Patton, J. M. C. Stork, B. S. Meyerson, D. L. Haramé, *Proc. IEE.* 1989, **36**, 2043–2064.
- (a) Y. F. Wu, B. P. Keller, S. Keller, D. Kopolnek, P. Kozodoy, S. P. Denbaars, U. K. Mishra, *Appl. Phys. Lett.* 1996, **69**, 1438–1440. (b) J. Wang, H. B. Wang, X. J. Yan, H. C. Huang, D. H. Yan, *Appl. Phys. Lett.* 2005, **87**, 093507-1-3.
- (a) A. Hagfeldt, G. Boschloo, L. C. Sun, L. Kloo, H. Pettersson, *Chem. Rev.* 2010, **110**, 6595–6663. (b) A. J. Heeger, *Adv. Mater.* 2014, **26**, 10–28. (c) Y. Huang, E. J. Kramer, A. J. Heeger, G. C. Bazan, *Chem. Rev.* 2014, **114**, 7006–7043.
- (a) C. W. Tang, S. A. VanSlyke, C. H. Chen, *J. Appl. Phys.* 1989, **65**, 3610–3616. (b) S. Wang, H. Zhang, B. Zhang, Z. Xie, W. Y. Wong, *Mat. Sci. Eng. R* 2020, **140**, 100547.
- (a) F. Huang, E. V. Anslyn, *Chem. Rev.* 2015, **115**, 6999–7000. (b) M. A. Boles, M. Engel, D. V. Talapin, *Chem. Rev.* 2016, **116**, 11220–11289. (c) S. Leininger, B. Olenyuk, P. J. Stang, *Chem. Rev.* 2000, **100**, 853–908. (d) G. M. Whitesides, B. Grzybowski, *Science* 2002, **295**, 2418–2421.
- (a) M. D. Gujrati, N. S. S. Kumar, A. S. Brown, B. Captain, J. N. Wilson, E. M. Engler, B. A. Scott, S. Etemad, T. Penney, V. V. Patel, *J. Am. Chem. Soc.* 1977, **99**, 5909. (b) R. Natarajan, G. Magro, L. N. Bridgland, A. Sirikulkajorn, S. Narayanan, L. E. Ryan, M. F. Haddow, A. Guy Orpen, J. P. H. Charmant, A. J. Hudson, A. P. Davis, *Angew. Chem. Int. Ed.* 2011, **50**, 11386. (c) J. Q. Zhang, Y. J. Zhang, J. Fang, K. Lu, Z. Y. Wang, W. Ma, Z. X. Wei, *J. Am. Chem. Soc.* 2015, **137**, 8176. (d) M. Dabros, P. R. Emery, V. R. Thalladi, *Angew. Chem. Int. Ed.* 2007, **46**, 4132. (e) K. Sada, K. Inoue, T. Tanaka, A. Epergyes, A. Tanaka, N. Tohnai, A. Matsumoto, M. Miyata, *Angew. Chem. Int. Ed.* 2005, **44**, 7059.
- E. M. Engler, B. A. Scott, S. Etemad, T. Penney, V. V. Patel, *J. Am. Chem. Soc.* 1997, **99**, 5909–5916.
- M. Dabros, P. R. Emery, V. R. Thalladi, *Angew. Chem. Int. Ed.* 2007, **119**, 4210–4213.
- (a) X. M. Xu, T. Xiao, X. Gu, X. J. Yang, S. V. Kershaw, N. Zhao, J. B. Xu, Q. Miao, *ACS Appl. Mater. Interfaces* 2015, **7**, 28019. (b) Y. Zhen, H. Tanaka, K. Harano, S. Okada, Y. Matsuo, E. Nakamura, *J. Am. Chem. Soc.* 2015, **137**, 2247–2252.
- W. Zhang, W. S. Jing, T. Fukushima, A. Saeki, S. Seki, T. Aida, *Science* 2011, **334**, 340–343.
- M.-J. Sun, Y. Liu, Y. Yan, R. Li, Q. Shi, Y. S. Zhao, Y.-W. Zhong, J. Yao, *J. Am. Chem. Soc.* 2018, **140**, 4269–4278.
- H. Zhang, Y. Lei, H. Wang, W.-Y. Wong, *J. Mater. Chem. C* 2020, **8**, 2669–2675
- Y. Lei, Y. Sun, L. Liao, S. T. Lee, W.-Y. Wong, *Nano Lett.* 2017, **17**, 695–701.
- Y. Lei, Y. Sun, Y. Zhang, H. Zhang, H. Zhang, Z. Meng, W.-Y. Wong, J. Yao, H. Fu, *Nat. Commun.* 2018, **9**, 4358.
- (a) X. Xu, B. Shan, S. Kalytchuk, M. Xie, S. Yang, D. Liu, S. V. Kershaw, Q. Miao, *Chem. Commun.* 2014, **50**, 12828–12831. (b) Y. Wu, J. Feng, X. Jiang, Z. Zhang, X. Wang, B. Su, L. Jiang, *Nat. Commun.* 2015, **6**, 6737–6746. (c) C. Wang, Y. Liu, Z. Ji, E. Wang, R. Li, H. Jiang, Q. Tang, H. Li, W. Hu, *Chem. Mater.* 2009, **21**, 2840–2845.
- (a) C. Xu, P. He, J. Liu, A. Cui, H. Dong, Y. Zhen, W. Chen, W. Hu, *Angew. Chem. Int. Ed.* 2016, **55**, 9519–9523. (b) H. Dong, L. D. Sun, L. D. Li, R. Si, R. Liu, C. H. Yan, *J. Am. Chem. Soc.* 2017, **139**, 18492–18495.
- (a) M. H. Liu, L. Zhang, T. Y. Wang, *Chem. Rev.* 2015, **115**, 7304–7397. (b) Y. Wang, J. Xu, Y. W. Wang, H. Y. Chen, *Chem. Soc. Rev.* 2013, **42**, 2930–2962.
- Q. Li, Z. Li, *Acc. Chem. Res.* 2020, **53**, 962–973.
- Y. Cheng, S. Liu, F. Song, M. Khorloo, H. Zhang, T. K. Kwok, W. Y. Lam, Z. He, B. Z. Tang, *Mater. Horiz.* 2019, **6**, 405–411.